Scilight

Photocatalysis

https://www.sciltp.com/journals/photocatalysis



Article

Check for updates

Enhanced Photocatalytic Activity of $Cs_3Bi_2Br_9$ Nanocrystals: Colloidal vs. Supported Architecture

Joel Monfort [1], Alessandro Ciccone [1], Raman Singh Lamba [2], Dung Nguyen [3,4], Andrey Ryzhikov [3,4], Julia Pérez-Prieto [1,*], Dmitry Aldakov [2,*] and Raquel E. Galian [1,*]

[1] Institute of Molecular Science (ICMOL), University of Valencia, 46980 Paterna, Spain
[2] Univ. Grenoble Alpes, CEA, CNRS, Grenoble INP, IRIG, SyMMES, STEP, 38000 Grenoble, France
[3] Univ. de Haute-Alsace, CNRS, Institut de Science des Matériaux de Mulhouse (IS2M), UMR 7361, Axe Matériaux à Porosité Contrôlée, F-68100 Mulhouse, France
[4] Université de Strasbourg, F-67000 Strasbourg, France
* Correspondence: julia.perez@uv.es (J.P.-P.); dmitry.aldakov@cea.fr (D.A.); raquel.galian@uv.es (R.E.G.)

How To Cite: Monfort, J.; Ciccone, A.; Lamba, R.S.; et al. Enhanced Photocatalytic Activity of $Cs_3Bi_2Br_9$ Nanocrystals: Colloidal vs. Supported Architecture. *Photocatalysis* **2026**, *2*(4), 10. https://doi.org/10.53941/photocatalysis.2026.100010

Received: 11 July 2026
Revised: 15 October 2026
Accepted: 19 October 2026
Published: 27 October 2026

Abstract: Lead-free halide nanocrystals have emerged as a sustainable alternative to lead halide perovskites materials; owing to their strong light absorption, low-toxicity and optimal bandgap for visible light driven applications. Herein, we aim to broaden the application of benzoyl bromide as Br-source in a modified hot-injection protocol for the synthesis of colloidal $Cs_3Bi_2Br_9$ nanocrystals (cCBB NCs). Moreover, for comparative purposes CBB NCs incorporated into the mesoporous silica SBA-15 were prepared. The photocatalytic performance of both systems was evaluated using the degradation of cationic organic dyes, such as methylene blue (MB) and rhodamine B (RhB), as model reactions. Notably, complete dye degradation was achieved at very short irradiation times, ca. 300 s for RhB in both colloidal and supported systems, the fastest rate reported up to now, mediated predominantly by anion superoxide as selective oxidizing agent. However, in the case of MB, its strong binding to CBB surface and incorporation into the SBA-15 pores limit the photodegradation process, which is proposed to occur via direct charge transfer and anion superoxide formation. This work highlights the importance of the CBB synthetic procedure and the dye adsorption behavior on the NCs surface or into the silica pores in determining the photocatalytic activity of bismuth halide NCs.

Keywords: lead-free halide; nanocrystals; hot injection; photocatalysis; mesoporous silica; dye degradation

1. Introduction

Recently, perovskite-based nanomaterials have emerged as an important class of semiconductor materials with unique optoelectronic properties for potential applications in photovoltaics, optoelectronics, and more recently in photocatalysis [1]. Lead halide perovskites (LHPs) with a typical structure of AMX_3, are among the most extensively explored perovskite materials. In this structure, "A" is a large cation, which could be organic ($CH_3NH_3^+$, $NH_2CHNH_2^+$) or inorganic (Cs^+), giving hybrid and inorganic structures, respectively; "M" is a smaller metallic cation (typically a divalent one [Pb^{2+}]) and "X" corresponds to halides (Cl^-, Br^- or I^-) [2]. However, due to the toxicity of Pb and the reduced stability of these materials towards external factors (polar solvent, light and heat), alternative perovskite-inspired nanomaterials have been developed, replacing the environmentally harmful Pb^{2+} cation with more benign elements, taking advantage of the structural versatility of metal halide perovskites [3]. In this sense, tin (Sn), antimony (Sb) and bismuth (Bi) are considered the most promising cation substitutes for lead [4].

Copyright: © 2026 by the authors. This is an open access article under the terms and conditions of the Creative Commons Attribution (CC BY) license (https://creativecommons.org/licenses/by/4.0/).
Publisher's Note: Scilight stays neutral with regard to jurisdictional claims in published maps and institutional affiliations.

Although the replacement of Pb^{2+} by divalent Sn^{2+} preserves the 3D crystalline structure and stoichiometry, the facile oxidation of Sn^{2+} to Sn^{4+} remains a major challenge, significantly limiting the implementation of Sn-based inorganic halide perovskites [5]. Interestingly, the replacement of Pb^{2+} by a trivalent cation such as Sb^{3+} or Bi^{3+} leads to the formation of vacancy-ordered $A_3B_2X_9$ perovskite-derived structures. Depending on the halide composition and crystal packing, these compounds can adopt 0D, 1D, or 2D structures. In the layered 2D polymorph (space group *P*3*m*1), every third Bi or Sb layer along the (111) plane of the 3D parent perovskite structure is removed to maintain charge neutrality [6], resulting in the $A_3B_2X_9$ stoichiometry (B = Sb^{3+} or Bi^{3+}).

In this context, $Cs_3B_2X_9$ perovskite-inspired nanomaterials have emerged as promising lead-free alternatives to lead halide perovskites. In particular, colloidal $Cs_3Bi_2X_9$ NCs have been successfully synthesized through hot-injection approach, which enables rapid nucleation and controlled growth under well-defined reaction conditions. Mohammed et al. were pioneers in the preparation of hexagonal-phase $Cs_3Bi_2I_9$ NCs using BiI_3 as halide precursor at moderate temperature ca. 100 °C [7] while Gamelin et al. reported the formation of hexagonal $Cs_3Bi_2Br_9$ nanoplatelets using trimethylsilyl bromide (TMSBr) as bromide precursor [8]. Later on, an injection-free heating-up synthesis was reported for the preparation of thermodynamically stable $Cs_3Bi_2Br_9$ NCs, which are favored at high reaction temperature, long reaction times and high oleic acid concentrations [9]. Building on these advances, Manna et al. [10] introduced an alternative synthetic strategy based on the use of benzoyl halides as halide precursors, providing enhanced stability and optical properties of the resulting $CsPbX_3$ NCs, ascribed to the formations of halide-rich environment. This protocol decorrelates the introduction of metal cations and halide ions in the synthesis compared to a classic approach where they are incorporated with the same chemical precursor [10]. This method has been successfully used for the synthesis of quasi-spherical $Cs_3Sb_2Br_9$ NCs [11]; however, it has not been yet examined for the preparation of $Cs_3Bi_2Br_9$ NCs.

Bismuth bromide nanocrystals exhibit higher stability in polar media and greater resistance to ambient degradation than lead halide perovskites [12]. In addition, their band-gap values of approximately 2.6 eV [13] make them attractive visible-light-responsive materials for photochemical applications [14–16]. In fact, $Cs_3Bi_2Br_9$ NCs were employed as photocatalysts for hydrogen evolution and CO_2 reduction [17], where their structural stability and defect-tolerant electronic properties contribute to efficient charge separation and redox activity; and selective organic transformations, including the photocatalytic oxidation of aromatic substrates such as toluene and related derivatives [18]. Within this broader framework, organic dyes degradation has been used to evaluate their photocatalytic performance, in which RhB and/or MB are usually employed as benchmark pollutants due to their environmental relevance and easy absorption spectroscopy monitoring [19]. Moreover, dye degradation kinetics provide a direct insight into interfacial charge transfer processes between the photocatalyst and the dye [20]. Recently, 2D $Cs_3Bi_2Br_9$ nanosheets prepared via anti-solvent methodology were used for various dyes degradation, requiring 90 min to reach 80–90% of RhB, MB, and methyl orange (MO) degradation in water, without any difference observed between the dyes [21]. Colloidal $Cs_3Bi_2Br_9$ NCs, prepared by hot-injection approach and drop-cast onto glass slide, led to a degradation efficiency of 87% for RhB after 2.5 h, with a first-order reaction kinetics with $k = 1.67 \times 10^{-2}$ min^{-1} [22]. However, as the reaction was performed in aqueous media, the photocatalyst could only be used for one cycle due to water-induced degradation [22]. To overcome these limitations, the incorporation of these NCs into suitable support has been proposed as an effective strategy to enhance their functional properties. In particular, ordered mesoporous silica (SiO_2) is an appealing candidate for this role due to its high surface area, chemical inertness, thermal stability, and ability to prevent aggregation of the active phase while promoting improved dispersion and accessibility of reactive sites [23,24]. Mesoporous silica materials have been used as templates to preserve the structural integrity of several types of nanomaterials, including lead and lead-free halide perovskites [25,26].

Herein, we report a comparative study of the photocatalytic performance of colloidal and supported Bi-based bromide nanocrystals through the degradation of organic dyes in isopropanol under aerobic conditions as model reaction. The use of benzoyl bromide in the hot-injection protocol enables the synthesis of colloidal $Cs_3Bi_2Br_9$ (cCBB) NCs exhibiting high photocatalytic activity toward the degradation of RhB and MB, achieving the shortest irradiation time reported to date. The incorporation of CBB within SBA-15 silica mesopores results in a robust photocatalyst that can be reused for at least five cycles for RhB. In contrast, for MB, the high adsorption of the dye on both the NCs surface and silica pores leads to a different photocatalytic performance.

2. Materials and Methods

2.1. Materials

Bismuth (III) bromide ($BiBr_3$, 98%; Sigma-Aldrich), bismuth (III) acetate ($Bi(CH_3CO_2)_3$, 99.9% trace metals basis; Sigma-Aldrich, St. Louis, MO, USA), cesium bromide (CsBr, 99.9%, metals basis; Alfa Aesar, Haverhill,

MA, USA), cesium carbonate (Cs_2CO_3, 99%; Sigma-Aldrich), dimethyl sulfoxide (DMSO, dried, 99.8%; Sigma-Aldrich), 2-propanol (IPA, 99.8%, for analysis; Scharlau, Sentmenat, Spain), hydrochloric acid (HCl, 37%; Carlo Erba, Cornaredo, Italy), 1-octadecene (ODE, 90%; Alfa-Aesar), oleylamine (OLA, 70%; Sigma-Aldrich), oleic acid (OA, 90%; Alfa Aesar), benzoyl bromide (Bz-Br, 97%; Sigma-Aldrich), ethyl acetate anhydrous (EtOAc, 99.8%; Sigma-Aldrich), triblock copolymer EO20PO70EO20 (Pluronic P123; Sigma-Aldrich), tetraethyl orthosilicate (TEOS, 98%; Sigma-Aldrich), toluene (99.8%; Sigma-Aldrich), rhodamine B (RhB, 99%; Sigma-Aldrich), methylene blue (MB, ≥97%; Sigma-Aldrich), 2,2,6,6-tetramethylpiperidine-1-oxyl (TEMPO, 98%; Sigma-Aldrich) and ferrocene (>95%; TCI, Tokyo, Japan). All chemicals and reagents were used as received from suppliers without any further purification.

2.2. Synthesis

2.2.1. Synthesis of $Cs_3Bi_2Br_9$ (cCBB) NCs

Colloidal $Cs_3Bi_2Br_9$ NCs were synthesized following the hot-injection approach with some modifications [27]. In a typical synthesis, Cs_2CO_3 (0.25 mmol, 82.3 mg), ODE (13.10 mmol, 4.6 mL), OLA (1.28 mmol, 0.6 mL), and OA (1.69 mmol, 3 mL) were placed in a 50 mL three-necked round-bottom flask inside a nitrogen atmosphere glove box, followed by the addition of Bi precursor ($Bi(CH_3CO_2)_3$, 0.331 mmol, 128 mg). The mixture was stirred and heated up to 160 °C under vacuum for 1h. Thereafter, 210 µL of benzoyl bromide (1.73 mmol) in 500 µL of degassed ODE was injected into the reaction mixture under nitrogen atmosphere, held for 30 s and then quenched in an ice-water bath, leading to a bright yellow product. The product was centrifuged using 4 mL of anhydrous ethyl acetate at 4000 rpm for 3 min and the solid obtained was discarded. The supernatant was centrifuged at 8000 rpm for 5 min, and the precipitate was dispersed in toluene and stored inside a glovebox for further characterization.

2.2.2. Synthesis of Mesoporous SiO_2 (SBA-15)

SBA-15 ordered mesoporous silica with unidimensional mesopores (pore size of 6.6 nm) and high specific surface area (S_{BET} = 1010 m^2 g^{-1}) was synthesized by dissolving (11 mmol, 4.0 g) of P123 in an acidic solution prepared from 23.28 g of 37% HCl and 127 mL of deionized water and stirred at 40 °C for 2h. Subsequently, TEOS (40.75 mmol, 9.1 mL) were added. The mixture was stirred at 35 °C for 4 h and then aged under static conditions at 95 °C for 24 h. The molar composition of the synthesis mixture was 1 TEOS:0.017 P123:5.68 HCl:190 H_2O.

2.2.3. Synthesis of $Cs_3Bi_2Br_9$@SBA-15 (CBB@SiO_2)

First, CsBr (1.05 mmol, 0.23 g) and $BiBr_3$ (0.7 mmol, 0.32 g) were dissolved in 2.5 mL of DMSO until a clear solution was obtained. This solution was subsequently filtered through a 0.45 µm PTFE filter prior to impregnation. The CBB@SBA-15 was prepared via a wet impregnation approach. For that, 62 µL of the 0.14 M $Cs_3Bi_2Br_9$ precursor solution was added to 100 mg of dried SBA-15 and gently mixed for 15 min using a pestle and mortar inside a glove box. Following impregnation, the powders were heated at 180 °C for 1 h in a furnace in ambient atmosphere. The synthesized materials were then stored under ambient conditions for subsequent characterization and photocatalytic studies.

2.3. Characterization Techniques

UV-Visible absorption measurements were carried out on a UV/VIS/NIR Lambda 1050 spectrophotometer (Shelton, CT, USA), equipped with the software PerkinElmer UV Winlab. The powder X-ray Diffraction (XRD) patterns of all samples were obtained on a Panalytical Empyrean X-ray platform (Malvern Panalytical, Almelo, The Netherlands) with capillary set-up and copper radiation (Cu Kα = 1.54178 Å). The capillary tube was made of special glass no. 0140, with diameters of 0.5 and 0.7 mm. Raman measurements were acquired using a Confocal Raman microscope (RMS1000, Edinburgh Instruments, Livingston, UK). The sample was irradiated using a 532 nm lased focused at 100×/0.9 N.A objective lens. Backscattered light was collected using an 800 mm focal length spectrograph with a 1200 g/mm grating, and the Raman spectra was recorded using an EM-CCD3 detector. Transmission Electron Microscopy (TEM) was performed on a JEOL Jem1010 microscope (JEOL Ltd., Tokyo, Japan) with a tungsten filament operated at 100 keV. High-Resolution TEM (HRTEM) images were performed on a FEI TECNAI G2 F20 (Thermo Fisher Scientific, Hillsboro, OR, USA), operated at 200 keV. All X-ray photoelectron (XPS) spectra were collected using a K-ALPHA (Thermo Scientific, East Grinstead, UK) equipment, monochromatized by a twin crystal monochromator, yielding a focused X-ray spot (elliptical in shape with a major axis length of 400 µm) at 3 mA × 12 kV. The alpha hemispherical analyzer operated in constant

energy mode with survey scan pass energies of 200 eV to measure the whole energy band and 50 eV in a narrow scan. XPS spectra were calibrated using C1s spectra (284.8 eV) and treated with the Avantage 5 software. Zeta potential measurements were conducted using Zetasizer Ultra (Malvern, UK) in a disposable capillary cell for zeta potential measurements (DTS1070). Thermogravimetric analyses were determined at a heating rate of 5 °C min^{-1} from 25 to 750 °C under air conditions using a TGA 550 (TA Instruments, New Castle, DE, USA). Gas Chromatography-Mass Spectrometry measurements were carried on a ZenoTOF 7600 (AB Sciex, Framingham, MA, USA) plus where chromatographic separation was performed using Exion UHPLC instrument (mobile phase at 0.1 mL/min H_2O:MeOH at 5 mM NH_4^+ format) equipped with an optiflow Electrospray Ionization (ESI) source (AB Sciex, Shanghai, China) and with a GC System (Agilent 8860, Agilent Technologies, Santa Clara, CA, USA) coupled to a mass detector (Agilent 5977 GC/MSD, Agilent Technologies, Santa Clara, CA, USA).

2.4. Photocatalytic Experiments

Photocatalytic experiments were conducted in a quartz cuvette using a PhD M2 photoreactor (Sigma-Aldrich) with a 420 nm LED as excitation source (radiometric power: 925 W; see Figure S1 for the LED emission spectrum). Briefly, the as-prepared colloidal Bi-based photocatalyst (0.4 mg cCBB) or supported one (3 mg CBB@SBA-15) was dispersed in 2 mL of IPA followed by the addition of RhB or MB organic dyes (7.30×10^{-5} mmol). The mixture was gently stirred in the dark for 30 min to establish adsorption-desorption equilibrium of the dyes onto the NCs surface. Subsequently, the cuvette was placed in the photoreactor and irradiated under continuous soft stirring. The reaction was monitored by measuring the absorbance at different time intervals for at least 15 min.

3. Results and Discussion

3.1. Synthesis and Characterization of cCBB NCs and CBB@SBA-15

Recently, a new protocol was developed for the hot-injection synthesis of $CsPbBr_3$ NCs using benzoyl bromide as Br-precursor, taking advantage of the independent control over the ratios Cs:Pb:Br and yielding the NCs with improved optical properties and stability [10]. Later, it was extended to the synthesis of $Cs_3Sb_2Br_9$ NCs with outstanding photocatalytic properties for organic transformation [11]. We decided to adapt and optimize this method to synthesize colloidal $Cs_3Bi_2Br_9$ (cCBB) NCs by dissolving cation precursors (bismuth acetate and cesium carbonate) in a mixture of oleylamine and oleic acid in 1-octadecene followed by a hot injection of a halide source (benzoyl bromide) at 160 °C (see Figure 1a and Experimental Section). For comparative purposes, the same CBB material but supported as NCs in mesoporous silica (CBB@SBA-15) was prepared using an impregnation/heating technique (see Figure 1b and Experimental Section).

UV-Vis absorption spectroscopy was employed to investigate the optical properties of the CBB NCs. Both materials exhibit a strong absorption feature at 440 nm (Figure 1c), similar to those reported for bulk crystals and thin films [22,28], as no significant effect on the spectral properties and band gap was expected due to a very low excitonic Bohr radius (<0.5 nm) and strong exciton binding energies [16,29]. Band gaps (E_g) of 2.51 and 2.58 eV were estimated from the Tauc plots (Figure S2) for cCBB NCs and CBB@SBA-15, respectively, in good agreement with previous reports [22,30]. Raman spectroscopy was performed to evaluate the crystalline properties of cCBB NCs in the 50–250 cm^{-1} region (Figure 1d). The vibration modes associated with bromide atoms (Br-Br) were observed as resolved weak bands at 65, 74, and 87 cm^{-1}; together with the two characteristic intense and sharp peaks at 162 and 187 cm^{-1} assigned to the $E1_g$ and $A1_g$ normal modes, arising from Bi–Br vibrations within the corner-sharing $[BiBr_6]^{3-}$ octahedra [30–33] similar to CBB@SBA-15. The full width at half maximum (FWHM) values of the $E1_g$ and $A1_g$ normal modes are indicative of the degree of crystallinity of the material [31]. cCBB NCs exhibited FWHM values of 7.4 and 7.7 cm^{-1} for the $E1_g$ and $A1_g$ modes, respectively, while CBB@SBA-15 showed values of 6.6 and 8 cm^{-1}, which are close to those reported for single crystals [31,32] confirming the high crystallinity of both NCs studied. Powder X-ray diffraction pattern for cCBB NCs is illustrated in Figure 1e. The peaks observed at 12.8° (100), 15.7° (011), 18.0° (002), 22.3° (110), 27.4° (003), 31.8° (022), 35.5° (121) and 39.2° (122) are consistent with the standard pattern (PDF #01-70-0493), lattice parameters of $a = 7.97200$ Å, $c = 9.86700$ Å and $P3m1$ hexagonal space group of vacancy-ordered 2D-layered $Cs_3Bi_2Br_9$ [2,3,33]. The XRD pattern of CBB@SBA-15 exhibits diffraction peaks at 12.8° (100), 15.6° (011), 17.9° (002), 27.2° (003), 31.8° (022), 35.5° (121) and 39.8° (122), which are consistent with those of cCBB NCs, indicating CBB@SBA-15 retain the same crystalline phase. CBB and SBA-15 [34]. To further characterize the cCBB NCs, XPS measurements were performed (Figure S3). XPS spectrum of Bi 4f displays two distinct peaks at 159.2 ($4f_{7/2}$) and 164.5 eV ($4f_{5/2}$), corresponding to the bismuth in bromide environment. The Br 3d spectrum exhibits two peaks at 68.3 and 69.3 eV, assigned to the Br $3d_{5/2}$ and $3d_{3/2}$, respectively, and corresponding to the Br^- state. For Cs 3d, two peaks at 724.5 ($3d_{5/2}$) and 739.5 eV ($3d_{3/2}$) correspond to the typical Cs chemical shift in bromide perovskites. TGA

analysis of cCBB NCs showed a 40% of the active inorganic CBB material (Figure S4a), while its loading in supported CBB@SBA-15 was estimated ca. 12% (*w*/*w*), according to the synthetic procedure (Figure S4c).

Transmission electron microscopy was used to study the morphology and crystallinity of the CBB NCs. The formation of quasi-spherical NCs with an average size of ca. 10.8 and 6.2 nm was confirmed for colloidal and supported CBB, respectively (Figure 2a,b). Importantly, CBB was efficiently formed inside the silica pores (Figure 2b, see Figure S5 for bare SBA-15). Well-defined lattice fringes of 3.11 and 3.65 Å, as well as 3.12 and 3.67 Å corresponding to the (003) and the (110) $Cs_3Bi_2Br_9$ planes [35,36] were observed for cCBB NCs and CBB@SBA-15, respectively. Collectively, these results confirm the high purity of the crystalline phase of cCBB NCs and the formation of CBB inside the SBA-15 pores.

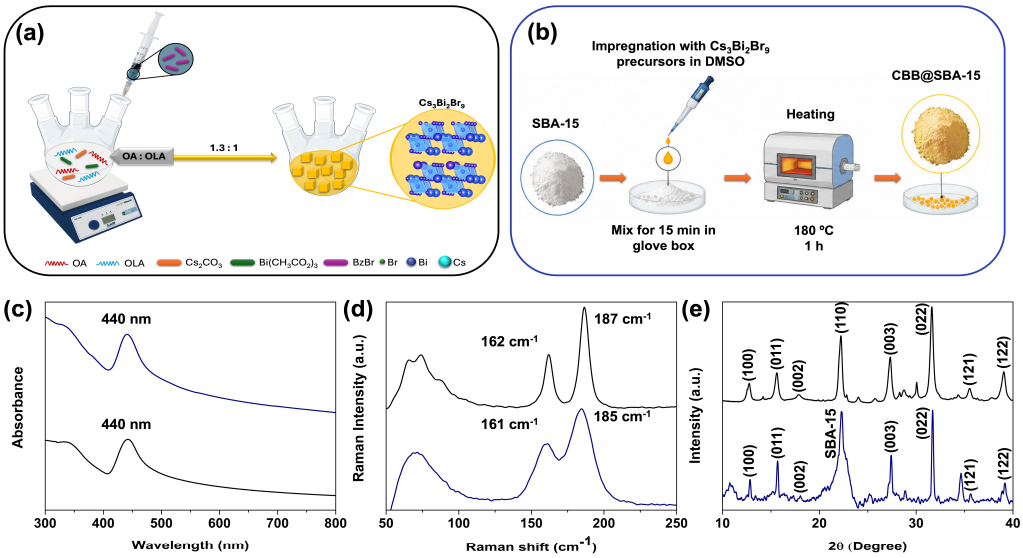


Figure 1. Synthetic protocol scheme for the preparation of (**a**) cCBB NCs and (**b**) CBB@SBA-15. (**c**) Absorption spectra of cCBB NCs (black line) and CBB@SBA-15 (blue line), in IPA. (**d**) Raman spectra of cCBB NCs and CBB@SBA-15, and (**e**) XRD spectra of cCBB NCs and CBB@SBA-15.

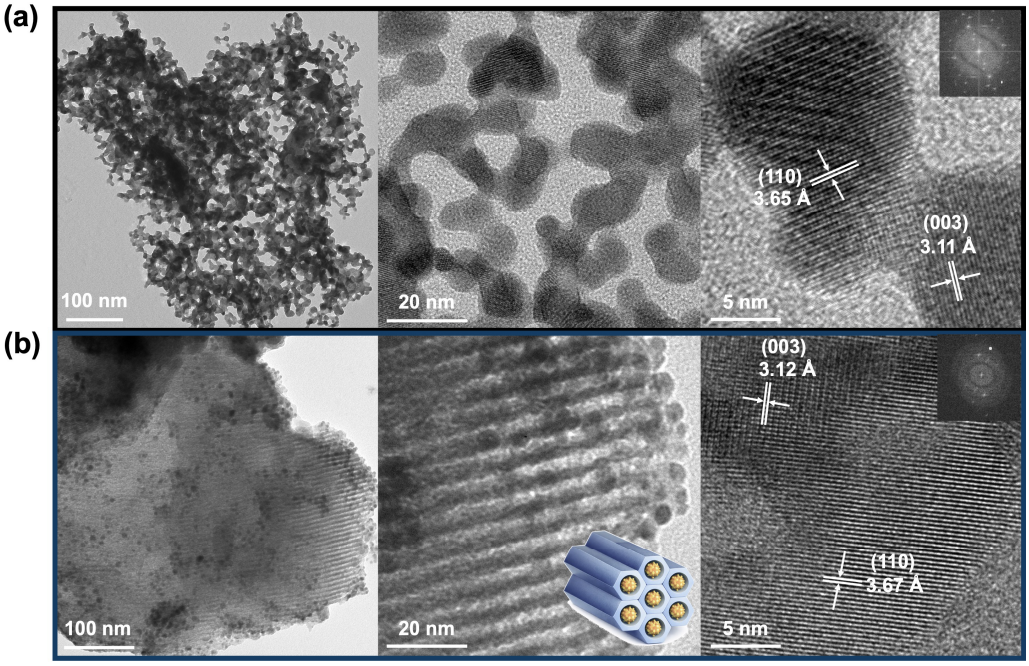


Figure 2. TEM and HRTEM images for (**a**) cCBB NCs and (**b**) CBB@SBA-15.

3.2. Photocatalytic Studies

The photocatalytic activity of semiconductor NCs for organic dyes degradation depends on dye-photocatalyst interactions, molecular structure of the dyes and the surface properties of the materials [31]. In this work, we aim

to study the role of dye adsorption on the surface of colloidal NCs and/or within silica pores on photocatalytic performance, efficiency, and degradation kinetics of the dye. In a typical experiment, the photocatalyst (with the amount adjusted to have 0.4 mg of photoactive CBB) was dispersed in IPA (2 mL) followed by the addition of the dyes (RhB or MB). First, the mixture was gently stirred in the dark to ensure proper adsorption-desorption equilibrium of the dye on the photocatalyst surface (Figure 3a,c). The photocatalytic process was monitored by following the absorption spectra of the dye solutions. The spectrum of RhB in the presence of cCBB NCs or CBB@SBA-15 after 30 min under dark conditions remained unchanged, suggesting a rapid establishment of adsorption equilibrium. Upon irradiation at 420 nm, the characteristic absorption peak of RhB at 550 nm progressively decreased in the presence of both photocatalysts, resulting in photodegradation efficiencies of 100% and 93% within only 300 s for cCBB NCs and CBB@SBA-15, respectively (Table 1), which is the highest reported in the literature among other Bi halide-based nanocrystals [14,31], same material prepared by conventional hot-injection [5] and other related materials [37]. Preparation of multifunctional composites can improve the photodegradation efficiency up to 97.4% but only after 60 min [38].

It is noteworthy that the adsorption of RhB into cCBB NCs and CBB@SBA-15 was only 5% and 12%, respectively, under dark conditions. However, the dominant process is the photodegradation as no residual RhB adsorption on the photocatalyst was detected in the absorption spectrum recorded after irradiation, with only the features of the cCBB NCs and CBB@SBA-15 observed (Figure S6a,b).

Table 1. Photocatalytic activity of cCBB NCs and CBB@SBA-15.

Material	Dye	Light source	Power	Irradiation	Degradation	Reference
$Cs_3Bi_2Br_9$	RhB	Solar Simulator	1000 W·m^{-2}	100 min	100%	[5]
	MB			100 min	99%	
	MB	UV	125 W	90 min	80%	[21]
	RhB	Visible light (LED 420 nm)	39 W·m^{-2}; 5.88 mV·cm^{-2}	270 s	100%	This work
	MB			11 min	100%	
$Cs_3Bi_2Br_9$/g-C_3N_4	MB	Solar Simulator	250 W·m^{-2}	60 min	100%	[39]
$Cs_3Bi_2Br_9$@SBA-15	RhB	Visible light (LED 420 nm)	39 W·m^{-2}; 5.88 mV·cm^{-2}	300 s	93%	This work
	MB			8 min	67%	

The photocatalytic degradation kinetics was analyzed using a pseudo-first-order Langmuir-Hinshelwood model (Equation (1)), where C_t and C_0 denote the dye concentration at irradiation time t and at t_0, respectively, and k is the apparent rate constant.

$$\ln\frac{C_t}{C_0} = -k.t \quad (1)$$

Rate constants of 1.4×10^{-2} and 1.1×10^{-2} s^{-1} were obtained for RhB in the presence of cCBB NCs and CBB@SBA-15, respectively (Figures 3b and S7). A slightly lower degradation rate for CBB@SBA-15 could be rationalized by the incorporation and diffusion of the RhB dye into the silica mesopores as the same amount of photoactive CBB was used.

To evaluate the recyclability of the photocatalysts, cCBB NCs or CBB@SBA-15 were recovered after each photocatalytic run, mixed with a fresh dye solution and subjected to a new irradiation cycle. Differences between the photocatalysts became apparent starting from the fourth cycle onward. While the photocatalytic performance of cCBB NCs decreased, dropping to ca. 33% for RhB degradation, CBB@SBA-15 can be reused at least 5 cycles preserving the high degradation efficiency (Figure 3b). The superior photocatalytic performance of supported CBB could be related to the cooperative action of the SiO_2 pores, available CBB facets in the pores, and close interaction between the dye and the NCs.

In the case of MB, a different behavior was observed. A significant decrease in the absorption spectrum of MB (33% for cCBB NCs and 85% for CBB@SBA-15) was already observed after 30 min under dark conditions (Figure 3c), indicating substantial adsorption of MB onto the photocatalysts. The strong affinity of the MB for the CBB surface with recently reported adsorption energy of 2.05 eV [40] may contribute to the efficient photodegradation. Indeed, a z-potential value of −7.8 mV was obtained for cCBB NCs (compared to −22 mV reported for CBB synthesized by mechanochemistry [31]), which is favorable for the adsorption of cationic MB.

To explain much stronger MB absorption drop in the dark in the presence of the supported CBB@SiO_2, we first compared the adsorption of RhB and MB dyes on pure SBA-15. While the former was negligible, that of MB/SiO_2 was 32% (Figure S8), which could be related to the larger molecular size of the RhB, limiting its penetration into the pores. Additionally, weaker charge of the RhB molecule can reduce its interaction with the silica. Indeed, the incorporation of MB on the mesoporous SiO_2 may be favored by electrostatic interactions

between the amine group of the dye and the Si-OH groups on the silica surface, as previously proposed for MB within porous silica nanoaggregates [41]. A z-potential of −0.3 mV measured for CBB@SBA-15 indicates a slightly negatively charged surface of the photocatalyst, favoring the interactions of cationic MB with both CBB and SBA-15. Interestingly, MB dimers have been reported to be the dominant adsorbed species in mesoporous silica [42], and their formation cannot be ruled out in our systems.

Under visible-light irradiation, cCBB NCs promoted high MB photodegradation, reaching 100% efficiency in 11 min (Table 1, Figure 3d) with a rate constant k of 0.20 min^{-1}. The absence of residual MB on the photocatalyst, even after 10 photocatalytic cycles, suggests that the adsorbed dye may undergo further degradation upon irradiation. In the case of CBB@SBA-15, adsorption of MB into the SBA-15 pores is proposed to be the primary mechanism responsible for the initial decrease in the dye absorption band. Accordingly, the real photodegradation efficiency was 67% (Figure 3d), with a constant rate of 0.10 min^{-1} (Figure S7). In all cases, the degradation values were calculated using the dye concentration measured after 30 min of dark adsorption. The overall dye decoloration efficiency, which includes both dye adsorption and photodegradation, reaches 95% in this case. However, differences in photocatalyst stability became evident upon recycling. cCBB NCs retained high photocatalytic activity throughout four consecutive cycles, with a dye degradation rate of up to 57% in the final cycle. In contrast, CBB@SBA-15 was active only during first two cycles (Figure 3d). The progressive loss of activity of the supported material may be attributed to the saturation of the silica mesopores by MB molecules, which may hinder further diffusion of the dye into the pores and block the access to the CBB surface active sites consequently limiting the photocatalytic activity. It is noteworthy that the photocatalytic efficiency of cCBB NCs was higher than that reported in other reports using CBB or CBB/g-C_3N_4 (Table 1).

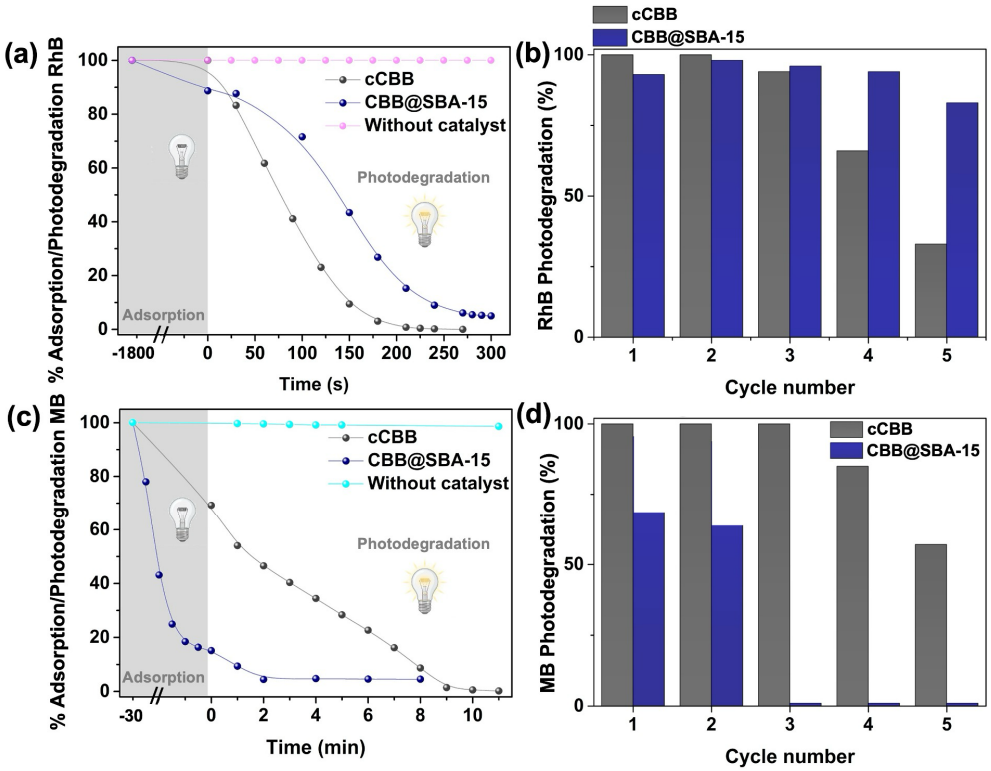


Figure 3. Photocatalytic activity of cCBB NCs and CBB@SBA-15 for (**a**) RhB and (**c**) MB degradation. Photodegradation cycles are illustrated in (**b**) for RhB and (**d**) for MB in the presence of cCBB NCs and CBB@SBA-15 in both cases.

These results reveal significant differences in the photocatalytic behavior of the studied systems under visible-light irradiation, and a series of additional experiments were conducted to gain insight into the dye degradation mechanism. First, a control photocatalytic reaction under dark conditions after reaching the adsorption-desorption equilibrium or in the absence of a photocatalyst resulted in a negligible effect on the absorption spectrum of both dyes, demonstrating that both the photocatalyst and light are required for the reaction progress.

Photocatalytic dye degradation mediated by semiconductor nanocrystals can proceed via direct photolysis of the dyes, photoredox reaction between the dye and the photocatalyst upon excitation of the semiconductor, and/or degradation by the formation of reactive oxygen species (ROS) [43]. The photocatalytic tests were carried out at

420 nm to selectively excite the photoactive CBB nanocrystals. Control experiments of the RhB and MB irradiation in the absence of CBB performed under the same irradiation conditions confirmed their high photostability, as evidenced by only negligible changes in the absorbance (Figures 3a,c and S9). To evaluate the feasibility of the photoredox reactions, the band alignment between CBB and the dyes was examined together with the reduction potential of anion superoxide (Figure 4a). The conduction and valence bands (Figure S10) of CBB were estimated by the combination of Tauc plots (Figure S2) and XPS measurements (Figure S3), while the HOMO and LUMO energy levels of the dyes were taken from the reported data [31,44]. For simplicity, the same Eg value was assumed for cCBB NCs and CBB@SBA-15. The valence band of CBB (−5.6 eV) is almost isoenergetic with the HOMO level in the case of MB, which could enable direct hole transfer from the semiconductor to the dye; while LUMO level below the CB of CBB indicates possible photoexcited electron transfer only for MB. It should be noted that the energies of isolated CBB and dyes are presented, while they can be shifted due to solvation. Moreover, previously, it was calculated that the MB adsorption on the CBB surface can shift both VB and CB of the latter [31] that could further slightly change the real band alignment.

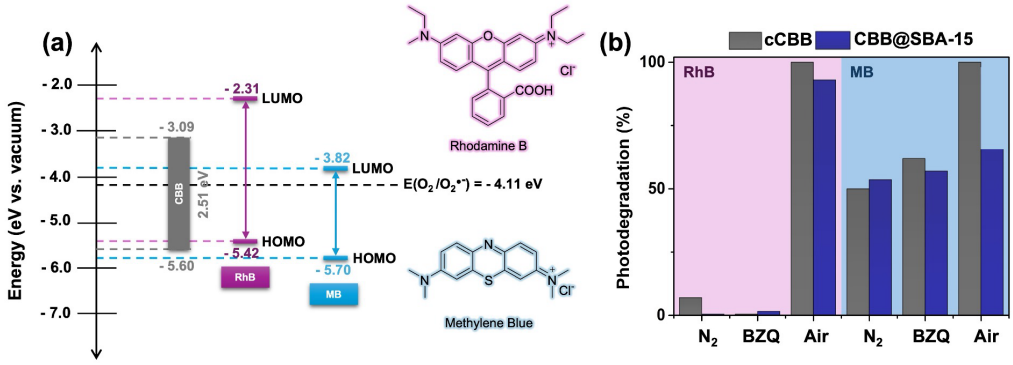


Figure 4. (**a**) Band alignment between CBB and dyes. (**b**) Photodegradation activity of both photocatalysts under different conditions.

Under aerobic conditions, the formation of anion superoxide ($O_2^{\bullet-}$) upon irradiation is highly probable and has been reported as the most common oxidative species for dye degradation [15,45,46]. In order to evaluate its participation in the degradation mechanism, the photocatalytic reaction was performed under nitrogen atmosphere to avoid the presence of oxygen and using benzoquinone (BZQ) as $O_2^{\bullet-}$ scavenger (Figure 4b). In the case of RhB, a marked inhibition of the photodegradation rate was observed under N_2 and in the presence of the BZQ for both cCBB NCs and CBB@SBA-15, suggesting that the anion superoxide is strongly involved in the dye photodegradation (Table 2). In contrast, 50–60% of photocatalytic activity was retained for MB under the same conditions, indicating the possibility of an alternative photodegradation mechanism. It is noteworthy that the formation of hydroxyl radicals (OH·) is ruled out in the presence of isopropanol, as it is a well-known scavenger of this species [47].

Table 2. Photocatalytic activity of cCBB NCs and CBB@SBA-15.

Photocatalyst	Dye	Atmosphere	Scavenger (10 eq.)	Photodegradation (%)
cCBB NCs	RhB	N_2	-	7
		Air	-	100
		Air	BZQ	0
		N_2	Ferrocene (h^+)	0
	MB	N_2	-	50
		Air	-	100
		Air	BZQ ($O_2^{\bullet-}$)	62
		N_2	Ferrocene (h^+)	61
		N_2	TEMPO (radical)	56
		N_2	$AgNO_3$ (e^-)	57
CBB@SBA-15	RhB	N_2	-	0
		Air	-	93
		Air	BZQ	2
	MB	N_2	-	54
		Air	-	67
		Air	BZQ	57

To further investigate the degradation mechanism, the photocatalytic reaction was carried out in the presence of a hole (ferrocene), radical (TEMPO), and electron scavengers ($AgNO_3$). In all cases, the MB photodegradation efficiency of ca. 50–60% was obtained, confirming that both $O_2^{\bullet-}$ and electron/holes contribute to the photodegradation of MB to a similar extent, while for RhB, ferrocene was also tested as a hole scavenger under nitrogen atmosphere, leading in a 0% photocatalytic degradation. This finding demonstrated that the degradation of RhB is mainly driven by $O_2^{\bullet-}$, with a minor contribution from holes (7%), which corresponds to the degradation percentage in the experiment carried out in N_2 conditions without the use of a hole scavenger (Table 2).

Degradation of RhB by ROS species usually includes *N*-deethylation, decarboxylation, and cleavage of the chromophore [48]. Notably, it has been reported that a hypsochromic shift of RhB absorption peak is associated with an *N*-deethylation process, which leads to a characteristic mass peak at *m*/*z* 415 in the Gas Chromatography-Mass Spectroscopy (GC-MS) analysis [49]. In our system, the intensity of the absorption peak of RhB was reduced with increasing irradiation times concomitant with a hypsochromic shift of 5 and 7 nm for cCBB NCs and CBB@SBA-15, respectively (Figure S6) suggesting the *N*-deethylation as a possible intermediate. According to the scavengers' tests (Table 2), the anion superoxide was proposed as the main ROS species responsible of the RhB photodegradation, which could be involved in the cleavage of the xanthene structure, leading to ring shortening and opening, and yielding aliphatic conjugated compounds and smaller intermediates [50,51]. In order to identify some intermediates of the photodegradation of RhB in the presence of cCBB NCs, we performed Electrospray Ionization Mass Spectrometry (ESI-MS) and Gas Chromatography-Mass Spectroscopy (GC-MS) analysis at 135 and 270 s of irradiation. Interestingly, the mass peaks at *m*/*z* 443 and 415 assigned to the *N*-deethylation intermediate of RhB dye, (Figure S11a) [51], were drastically reduced after 270 s (Figure S11b), in agreement with the rapid degradation of the dye. Moreover, the mass peak of *m*/*z* of 282 observed by ESI-MS or 281 by GC-MS (Figure S12) has been previously observed and assigned to the isomerized intermediate formed by *N*-deethylation, followed by carboxylation [52]. Collectively, our results suggest that the absorbance decrease of RhB corresponds to the photooxidation of the RhB dye, with *N*-deethylation being one of the main photodegradation pathways. Further oxidation of these intermediates produced progressively smaller molecules, that could eventually lead to mineralization.

According to the scavenger test, in the case of MB, the plausible electron transfer from CBB to the dye may lead to the formation of leucomethylene blue, which has been reported as a crucial intermediate in the degradation process in the reduction of MB by ascorbic acid [53].

The stability of the photocatalysts after one photocatalytic cycle was evaluated using optical and microscopy techniques. After the photodegradation of RhB, the absorption spectra of cCBB NCs and CBB@SBA-15 showed similar profile before (Figure 1) and after irradiation (Figure S13a,b) However, in the case of MB an absorption peak at ca. 660 nm is identified after the first photocatalytic cycle for both cCBB NCs and CBB@SBA-15 (Figure S13a,b) in agreement with the high affinity of the dye to NCs surface and the silica pores, respectively. Remarkably, the crystalline structure and morphology of both photocatalysts were preserved as illustrated in Figures S13c,d and S14. Several additional post-mortem experiments were performed to better elucidate that loss of activity in MB degradation using CBB@SBA-15 as photocatalyst. The Raman spectrum after the three photocatalytic cycles confirmed that the crystalline structure of CBB@SBA-15 was mainly preserved (Figure S15c). However, a slight broadening of the peaks at 160 cm^{-1} and 184 cm^{-1} was observed, which may be associated with the accumulation of MB in the pores and/or the silica surface. The recovered solid exhibited a green color, consistent with the presence of both the photocatalyst and residual adsorbed MB. Indeed, several washing steps were insufficient to completely remove the dye, suggesting a strong interaction between MB and CBB@SBA-15 (Figure S15a, inset). This observation was further supported by XPS spectroscopy revealing the presence of N 1s peak and increase of C 1s peak after three photocatalytic cycles indicating the accumulation of the dye on the photocatalyst (*vide supra*) that can be associated with reduction of its photocatalytic activity (Figure S15a,b). Furthermore, the C:Si atomic ratio almost doubles from 0.12 (before photocatalysis) to 0.21 (after photocatalysis), which evidences the adsorption of the organic dye within the pores and/or surface of the SBA-15 after three cycles. These results suggest that the progressive loss of activity was mainly associated with the dye accumulation and progressive pore blockage, while the structural integrity of the photocatalyst was preserved.

Moreover, we have evaluated the performance of the cCBB NCs photocatalyst after 10 photocatalytic cycles of MB irradiation. Interestingly, the absorption and the Raman spectra were maintained in agreement with the good stability of the optical and structural properties, while TEM showed similar morphology to pristine cCBB NCs but with higher aggregation (Figure S16). These findings suggest that the lower photocatalytic activity after several cycles could be ascribed to the organic ligand's loss, as previously observed for other colloidal perovskite nanocrystals [11].

4. Conclusions

In summary, we developed a new synthesis of colloidal $Cs_3Bi_2Br_9$ NCs by using benzoyl bromide as bromide precursor. The NCs were characterized and demonstrated the highest photocatalytic performance reported to date for the degradation of RhB and MB dyes used as model pollutants. We then compared the performance of these colloidal NCs with the $Cs_3Bi_2Br_9$ confined in the SiO_2 pores. The supported NCs exhibited enhanced stability during RhB degradation, whereas the strong affinity of the MB dye for the NCs surface and silica pores reduced the recyclability and limited the overall photocatalytic activity, highlighting the key role of dye-nanocrystal interaction at the interface. Importantly, the anion superoxide $O_2^{\bullet-}$ was found to be mainly responsible for the photodegradation of RhB with a small contribution of holes, whereas both photo-redox processes and $O_2^{\bullet-}$ contribute to the photodegradation of MB. The photocatalysts retained their performance over multiple cycles, with the NCs preserving their crystallinity and morphology. Overall, this study contributes to the better understanding of the superior photocatalytic activity of $Cs_3Bi_2Br_9$ NCs and opens the door to explore other types of photocatalytic reactions, including organic transformations.

Supplementary Materials

The additional data and information can be downloaded at: https://media.sciltp.com/articles/others/2610270950223452/Photocatalysis-26070112-SM.pdf. Figure S1. Emission spectrum of the LED centered at 420 nm used in photocatalytic experiments. Figure S2. Tauc plot for indirect band gap calculated using the Kubelka Munk function for (a) cCBB NCs and (b) CBB@SBA-15. Figure S3. XPS of (a) Cs3d; (b) Bi4f; and (c) Br3d of cCBB NCs. Figure S4. (a) TGA and (b) TGA first derivative curves of cCBB NCs. (c) TGA curves of CBB@SBA-15. Figure S5. HRTEM image of bare SBA-15 (Scale bar 20 nm). Figure S6. Photodegradation cycles of (a) cCBB NCs + RhB; (b) CBB@SBA-15 + RhB; (c) cCBB NCs + MB; and (d) CBB@SBA-15 + MB. (t_0 corresponds to the absorbance spectrum after 30 min of soft stirring in dark conditions). Figure S7. Plots of $\ln(C/C_0)$ versus time fitted using the pseudo-first-order Langmuir-Hinshelwood model for (a) cCBB NCs + RhB; (b) CBB@SBA-15 + RhB; (c) cCBB NCs + MB; and (d) CBB@SBA-15 + MB. Figure S8. Control experiment in the presence of SBA-15 (without any photocatalyst) for (a) RhB and (b) MB. (t_0 corresponds to the absorbance spectrum after 30 min of soft stirring in dark conditions). Figure S9. Absorbance spectra of (a) RhB and (b) MB upon irradiation with a LED at 420 nm for 300 s and 20 min, respectively. (t_0 corresponds to the absorbance spectrum after 30 min of soft stirring in dark conditions). Figure S10. Valence band estimation for cCBB NCs from XPS measurements. Figure S11. ESI-MS spectra of the photodegradation of RhB in the presence of cCBB NCs after (a) 135 sec and (b) 270 sec of reaction. Figure S12. GC-MS chromatogram of the photocatalytic degradation of RhB in the presence of cCBB NCs after (a) 135 sec and (b) 270 sec of the irradiation. (c) Mass spectrum of the peak at 8.718, which corresponds to m/z = 281. Figure S13. (a,b) Absorbance and (c,d) Raman spectra after 1 photocatalytic cycle for RhB and MB. Figure S14. TEM images of (a) cCBB NCs + RhB; (b) CBB@SBA-15 + RhB; (c) cCBB NCs + MB; and (d) CBB@SBA-15 + MB after one photocatalytic cycle. Figure S15. (a) High resolution of N1s; (b) survey XPS spectra; and (c) Raman spectra of the samples before and after 3 photocatalytic cycles of MB photodegradation with CBB@SBA-15. Figure S16. (a) Absorption spectra; (b) Raman spectra of the cCBB NCs before and after the 10th photocatalytic cycle of irradiation; (c,d) TEM images after the 10th photocatalytic cycle.

Author Contributions

D.A. and R.E.G.: conceptualization, methodology; J.M. and A.C: data curation, writing—original draft preparation; J.M., A.C., D.N. and R.S.L.: visualization, investigation; D.A., A.R. and R.E.G.: supervision; J.P.-P., D.A. and R.E.G.: writing—reviewing and editing. All authors have read and agreed to the published version of the manuscript.

Funding

This work was funded by Generalitat Valenciana (IDIFEDER/2018/064, IDIFEDER/2021/064, and CIPROM/2022/57), MINECO, grant number PID2023-152131NB-I00, Agencia Estatal de Investigación-AEI, grant number MMCIU Unit of Excellence "Maria de Maeztu" CEX2024-001467-M, French National Research Agency (grant ANR-23-CE09-0013 EncaPer) and European Union, European HORIZON MSCA Staff Exchange project: Advanced Multidisciplinary Research for Antimicrobial Resistance (AMRAMR 101131231).

Institutional Review Board Statement

Not applicable.

Informed Consent Statement

Not applicable.

Data Availability Statement

Data will be made available on request.

Acknowledgments

We thank M. Sales Galletero for her assistance and support with mass spectrometry measurements at the Servei Central de Suport a la Investigació Experimental (SCSIE) of the Universitat de València.

Conflicts of Interest

The authors declare no conflict of interest.

Use of AI and AI-Assisted Technologies

No AI tools were utilized for this paper.

References

1. Dey, A.; Ye, J.; De, A.; et al. State of the Art and Prospects for Halide Perovskite Nanocrystals. *ACS Nano* **2021**, *15*, 10775–10981. https://doi.org/10.1021/acsnano.0c08903.
2. Protesescu, L.; Yakunin, S.; Bodnarchuk, M.I.; et al. Nanocrystals of Cesium Lead Halide Perovskites ($CsPbX_3$, X = Cl, Br, and I): Novel Optoelectronic Materials Showing Bright Emission with Wide Color Gamut. *Nano Lett.* **2015**, *15*, 3692–3696. https://doi.org/10.1021/nl5048779.
3. Akinbami, O.; Majola, T.; Ngubeni, G.N.; et al. $CsSnBr_3$ and $Cs_3Bi_2Br_9$: Structural, Optical Characteristics, and Application in a Schottky Barrier Diode. *Adv. Photonics Res.* **2024**, *5*, 2300337. https://doi.org/10.1002/adpr.202300337.
4. Giustino, F.; Snaith, H.J. Toward Lead-Free Perovskite Solar Cells. *ACS Energy Lett.* **2016**, *1*, 1233–1240. https://doi.org/10.1021/acsenergylett.6b00499.
5. Akinbami, O.; Moepya, R.; Ngubeni, G.N.; et al. Lead-Free Rudorffite-Type $Cs_3Bi_2Br_9$ Nanoparticles for Photocatalytic Degradation of Rhodamine B and Methylene Blue. *J. Photochem. Photobiol. A Chem.* **2021**, *419*, 113460. https://doi.org/10.1016/j.jphotochem.2021.113460.
6. Akkerman, Q.A.; Manna, L. What Defines a Halide Perovskite? *ACS Energy Lett.* **2020**, *5*, 604–610. https://doi.org/10.1021/acsenergylett.0c00039.
7. Zhang, Y.; Yin, J.; Parida, M.R.; et al. Direct-Indirect Nature of the Bandgap in Lead-Free Perovskite Nanocrystals. *J. Phys. Chem. Lett.* **2017**, *8*, 3173–3177. https://doi.org/10.1021/acs.jpclett.7b01381.
8. Creutz, S.E.; Liu, H.; Kaiser, M.E.; et al. Structural Diversity in Cesium Bismuth Halide Nanocrystals. *Chem. Mater.* **2019**, *31*, 4685–4697. https://doi.org/10.1021/acs.chemmater.9b00640.
9. Lee, D.; Kim, M.; Woo, H.Y.; et al. Heating-up Synthesis of Cesium Bismuth Bromide Perovskite Nanocrystals with Tailored Composition, Morphology, and Optical Properties. *RSC Adv.* **2020**, *10*, 7126–7133. https://doi.org/10.1039/c9ra10106c.
10. Imran, M.; Caligiuri, V.; Wang, M.; et al. Benzoyl Halides as Alternative Precursors for the Colloidal Synthesis of Lead-Based Halide Perovskite Nanocrystals. *J. Am. Chem. Soc.* **2018**, *140*, 2656–2664. https://doi.org/10.1021/jacs.7b13477.
11. Rosa-Pardo, I.; Zhu, D.; Cortés-Villena, A.; et al. The Dark Side of Lead-Free Metal Halide Nanocrystals: Substituent-Modulated Photocatalytic Activity in Benzyl Bromide Reduction. *ACS Energy Lett.* **2023**, *8*, 2789–2798. https://doi.org/10.1021/acsenergylett.3c00771.
12. Jang, W.J.; Park, P.J.; Ong, W.J.; et al. Stable and Eco-Friendly Inorganic Lead-Free Perovskite Solar Cells: Structural, Electronic, and Defect Engineering. *Commun. Mater.* **2026**, *7*, 110. https://doi.org/10.1038/s43246-026-01158-1.
13. Bass, K.K.; Estergreen, L.; Savory, C.N.; et al. Vibronic Structure in Room Temperature Photoluminescence of the Halide Perovskite $Cs_3Bi_2Br_9$. *Inorg. Chem.* **2017**, *56*, 42–45. https://doi.org/10.1021/acs.inorgchem.6b01571.
14. Li, Y.J.; Mu, B.H.; Li, H.B.; et al. Bi-Based Metal Halide Perovskites and Their Photocatalytic Properties: A Review. *Energy Fuels* **2025**, *39*, 2986–3007. https://doi.org/10.1021/acs.energyfuels.4c06208.
15. Yue, T.; Zhang, S.Z.; Li, M.M.; et al. Lead-Free $Cs_3Bi_2Br_9$ Perovskite as Heterogeneous Photocatalyst for Oxidative Dehydrogenative Coupling of Thiols and P(O)H Compounds. *ChemSusChem* **2025**, *18*, e202501607. https://doi.org/10.1002/cssc.202501607.
16. Wang, C.; Ding, Y.; Liu, B.; et al. Crystal Structure Engineering of Metal Halide Perovskites for Photocatalytic Organic Synthesis. *Chem. Commun.* **2023**, *59*, 3122–3125. https://doi.org/10.1039/d3cc00468f.

17. Cui, X.; Zhang, Z.; Zhou, G.; et al. $Cs_3Bi_2Br_9$ and BiOBr Self-Assemble to Form S-Scheme Heterojunction for Photocatalytic CO_2 Photoreduction. *J. Alloys Compd.* **2026**, *1079*, 189779. https://doi.org/10.2139/ssrn.6674165.
18. Fan, Q.; Guo, L.; Wu, G.; et al. Ce^{3+}-Doped $Cs_3Bi_2Br_9$ for Photocatalytic Selective Oxidation of Alcohols to Aldehydes/Ketones. *Inorg. Chem.* **2026**, *65*, 1852–1862. https://doi.org/10.1021/acs.inorgchem.5c04499.
19. Ahmadi, B.; Fallah, A.; Ghamarpoor, R.; et al. Methylene Blue beyond the Dye: A Critical Review on Its Role as a Benchmark Pollutant in Photocatalyst Design. *Results Chem.* **2025**, *18*, 102910. https://doi.org/10.1016/j.rechem.2025.102910.
20. Pandey, M.; Tsunoji, N.; Bhattacharyya, K.; et al. Photocatalytic Degradation of Organic Dyes under Sunlight Using a Mononuclear Zn Complex-Embedded-Functionalized Porous Material. *Environ. Sci. Pollut. Res.* **2024**, *31*, 63686–63703. https://doi.org/10.1007/s11356-024-35466-1.
21. Masri, M.; Girisha, K.B.; Hezam, A.; et al. Enhanced Photocatalytic Activity and Stability of 2D $Cs_3Bi_2Br_9$ Perovskite Nanosheets Synthesized via Modified Antisolvent Method. *Colloids Surf. C Environ. Asp.* **2024**, *2*, 100024. https://doi.org/10.1016/j.colsuc.2023.100024.
22. Aragon, A.G.; Wiggins, T.E.; Ma, X.; et al. Lead-Free $Cs_3Bi_2Br_9$ and Cs_3Bi_2-xSbxBr$_9$ Nanocrystals as Photocatalysts with Enhanced Activity for the Degradation of Rhodamine in Aqueous Environments. *J. Photochem. Photobiol. A Chem.* **2023**, *436*, 114391. https://doi.org/10.1016/j.jphotochem.2022.114391.
23. Motokura, K.; Ding, S.; Usui, K.; et al. Enhanced Catalysis Based on the Surface Environment of the Silica-Supported Metal Complex. *ACS Catal.* **2021**, *11*, 11985–12018. https://doi.org/10.1021/acscatal.1c03426.
24. Malgras, V.; Tominaka, S.; Ryan, J.W.; et al. Observation of Quantum Confinement in Monodisperse Methylammonium Lead Halide Perovskite Nanocrystals Embedded in Mesoporous Silica. *J. Am. Chem. Soc.* **2016**, *138*, 13874–13881. https://doi.org/10.1021/jacs.6b05608.
25. Athira, M.P.; Haridas, S. Functionalized SBA-15 as a Protective Template for $CsPbBr_3$ Perovskite Quantum Dots. *Nanoscale Adv.* **2026**, *8*, 829–834. https://doi.org/10.1039/d5na00868a.
26. Dupé, S.; Liu, D.; Ghosh, A.; et al. Quantum-Confined Bismuth Iodide Perovskite Nanocrystals in Mesoporous Matrices. *Nanoscale* **2024**, *16*, 11223–11231. https://doi.org/10.1039/d4nr00430b.
27. Geng, H.; Huang, Z.; Geng, H.; et al. Controlled Synthesis of Highly Stable Lead-Free Bismuth Halide Perovskite Nanocrystals: Structures and Photophysics. *Sci. China Mater.* **2023**, *66*, 2079–2089. https://doi.org/10.1007/s40843-022-2299-6.
28. Yao, M.M.; Jiang, C.H.; Yao, J.S.; et al. General Synthesis of Lead-Free Metal Halide Perovskite Colloidal Nanocrystals in 1-Dodecanol. *Inorg. Chem.* **2019**, *58*, 11807–11818. https://doi.org/10.1021/acs.inorgchem.9b01893.
29. Tran, M.N.; Cleveland, I.J.; Aydil, E.S. Resolving the Discrepancies in the Reported Optical Absorption of Low-Dimensional Non-Toxic Perovskites, $Cs_3Bi_2Br_9$ and Cs_3BiBr_6. *J. Mater. Chem. C* **2020**, *8*, 10456–10463. https://doi.org/10.1039/d0tc02783a.
30. Mala, M.; Appadurai, T.; Chandiran, A.K. Structural Distortion Induced Broad Emission in Vacancy-Ordered Halide Triple Perovskites. *Dalton Trans.* **2022**, *51*, 2789–2797. https://doi.org/10.1039/d1dt03474j.
31. Azmat, S.; Gregori, L.; Ventruti, G.; et al. A Closer Look at the Interface of $Cs_3Bi_2Br_9$ Lead Free Perovskite in Photocatalytic Process. *J. Phys. Chem. Solids* **2025**, *199*, 112534. https://doi.org/10.1016/j.jpcs.2024.112534.
32. Bonomi, S.; Galinetto, P.; Patrini, M.; et al. Optical and Structural Property Tuning in Physical Vapor Deposited Bismuth Halides $Cs_3Bi_2(I_{1-X}Br_X)_9$ ($0 \leq X \leq 1$). *Inorg. Chem.* **2021**, *60*, 14142–14150. https://doi.org/10.1021/acs.inorgchem.1c01545.
33. Zhang, J.; Yang, Y.; Deng, H.; et al. High Quantum Yield Blue Emission from Lead-Free Inorganic Antimony Halide Perovskite Colloidal Quantum Dots. *ACS Nano* **2017**, *11*, 9294–9302. https://doi.org/10.1021/acsnano.7b04683.
34. Nguyen, Q.N.K.; Yên, N.T.; Hau, N.D.; et al. Synthesis and Characterization of Mesoporous Silica SBA-15 and ZnO/SBA-15 Photocatalytic Materials from the Ash of Brickyards. *J. Chem.* **2020**, *2020*, 1–8. https://doi.org/10.1155/2020/8456194.
35. Joshi, S.; Singh, N.; Singh, B.; et al. Lysine-Capped Bi-Based Halide Perovskite ($Cs_3Bi_2Br_{9-X}I_X$, X = 0, 3, 9) Nanoparticles: Unraveling Structure–Property–Function Relationship upon Halide Substitution. *ACS Appl. Nano Mater.* **2026**, *9*, 5381–5391. https://doi.org/10.1021/acsanm.5c05717.
36. Sunny, F.; John, S.; Parambil, P.C.; et al. Monovalent Cation Doping in Cesium Bismuth Bromide Perovskites: Insights into Structure–Property Correlation. *J. Phys. Chem. C* **2026**, *130*, 3135–3144. https://doi.org/10.1021/acs.jpcc.5c08110.
37. Yang, H.; Song, X.; Cheng, Z.; et al. Synergistic Catalysis for Advanced Water Treatment Enabled by Precisely Constructed Ag–O–Bi Asymmetric Active Sites. *Adv. Sustain. Syst.* **2026**, *10*, e70503. https://doi.org/10.1002/adsu.70503.
38. Li, S.; Li, J.; Ren, W.; et al. Schottky-Mediated Porphyrin-Metal-Organic Framework/Ti_3C_2-MXene Heterojunction for Water Decontamination via Photonic-Thermal-Enzyme Synergistic Catalysis. *J. Colloid Interface Sci.* **2025**, *691*, 137462. https://doi.org/10.1016/j.jcis.2025.137462.

39. Romani, L.; Speltini, A.; Dibenedetto, C.N.; et al. Experimental Strategy and Mechanistic View to Boost the Photocatalytic Activity of $Cs_3Bi_2Br_9$ Lead-Free Perovskite Derivative by g-C_3N_4 Composite Engineering. *Adv. Funct. Mater.* **2021**, *31*, 2104428. https://doi.org/10.1002/adfm.202104428.
40. Alarcos, N.; Cohen, B.; Ziółek, M.; et al. Photochemistry and Photophysics in Silica-Based Materials: Ultrafast and Single Molecule Spectroscopy Observation. *Chem. Rev.* **2017**, *117*, 13639–13720. https://doi.org/10.1021/acs.chemrev.7b00422.
41. Saita, S.; Anzai, M.; Mori, N.; et al. Controlled Aggregation of Methylene Blue in Silica–Methylene Blue Nanocomposite for Enhanced $^1O_2$ Generation. *Colloids Surf. A Physicochem. Eng. Asp.* **2021**, *617*, 126360. https://doi.org/10.1016/j.colsurfa.2021.126360.
42. Gupta, R.; Rastogi, P.K.; Srivastava, U.; et al. Methylene Blue Incorporated Mesoporous Silica Microsphere Based Sensing Scaffold for the Selective Voltammetric Determination of Riboflavin. *RSC Adv.* **2016**, *6*, 65779–65788. https://doi.org/10.1039/c6ra12336h.
43. Franchi, D.; Amara, Z. Applications of Sensitized Semiconductors as Heterogeneous Visible-Light Photocatalysts in Organic Synthesis. *ACS Sustain. Chem. Eng.* **2020**, *8*, 15405–15429. https://doi.org/10.1021/acssuschemeng.0c05179.
44. Hagberg, D.P.; Marinado, T.; Karlsson, K.M.; et al. Tuning the HOMO and LUMO Energy Levels of Organic Chromophores for Dye Sensitized Solar Cells. *J. Org. Chem.* **2007**, *72*, 9550–9556. https://doi.org/10.1021/jo701592x.
45. Ding, L.; Hou, Y.; Liu, H.; et al. Alcohols as Scavengers for Hydroxyl Radicals in Photocatalytic Systems: Reliable or Not? *ACS ES T Water* **2023**, *3*, 3534–3543. https://doi.org/10.1021/acsestwater.3c00271.
46. Nguyen, H.T.; Doan, V.D.; Huong Nguyen, T.L.; et al. Mechanistic Pathway and Optimization of Rhodamine B Degradation Using Mn_3O_4/ZnO Nanocomposite on Microalgae-Based Carbon. *RSC Adv.* **2025**, *15*, 6241–6259. https://doi.org/10.1039/d5ra00625b.
47. Basuki, T.; Nakashima, S.; Philo, D.; et al. Temperature-Directed Synthesis of Hematite-Goethite Nanocomposites Having Mild Self-Leaching Properties with Enhanced Photocatalytic Activity Involving Photo-Fenton Mechanism. *ChemistrySelect* **2026**, *11*, e06971. https://doi.org/10.1002/slct.202506971.
48. Tan, S.N.; Yuen, M.L.; Ramli, R.A. Photocatalysis of Dyes: Operational Parameters, Mechanisms, and Degradation Pathway. *Green Anal. Chem.* **2025**, *12*, 100230. https://doi.org/10.1016/j.greeac.2025.100230.
49. Phuruangrat, A.; Thungprasert, S.; Sakhon, T.; et al. Degradation of Rhodamine B Photocatalyzed by Eu-Doped CdS Nanowires Illuminated by Visible Radiation. *J. Indian Chem. Soc.* **2022**, *99*, 100349. https://doi.org/10.1016/j.jics.2022.100349.
50. Gao, Y.; Yang, G.; Zhang, J.; et al. A Metal-Free Microwave-Induced Carbon Cloth Discharge Technology for Efficient Degradation of Rhodamine B. *J. Environ. Manag.* **2026**, *411*, 130215. https://doi.org/10.1016/j.jenvman.2026.130215.
51. Yang, J.; Zhu, H.; Peng, Y.; et al. Photocatalytic Performance and Degradation Pathway of Rhodamine B with TS-1/C_3N_4 Composite under Visible Light. *Nanomaterials* **2020**, *10*, 756. https://doi.org/10.3390/nano10040756.
52. Rajalakshmi, S.; Pitchaimuthu, S.; Kannan, N.; et al. Enhanced Photocatalytic Activity of Metal Oxides/β-Cyclodextrin Nanocomposites for Decoloration of Rhodamine B Dye under Solar Light Irradiation. *Appl. Water Sci.* **2017**, *7*, 115–127. https://doi.org/10.1007/s13201-014-0223-5.
53. Majeed, A.; Ibrahim, A.H.; Al-Rawi, S.S.; et al. Green Organo-Photooxidative Method for the Degradation of Methylene Blue Dye. *ACS Omega* **2024**, *9*, 12069–12083. https://doi.org/10.1021/acsomega.3c09989.